Contents lists available at ScienceDirect

Nuclear Instruments and Methods in Physics Research A

Classification of bones from MR images in torso PET-MR imaging using a statistical shape model

Mohammad Reza Ay [a,b,*], Afshin Akbarzadeh [a,b], Alireza Ahmadian [a,c], Habib Zaidi [d,e,f]

[a] Research Center for Molecular and Cellular Imaging, Tehran University of Medical Sciences, Tehran, Iran
[b] Department of Medical Physics and Biomedical Engineering, Tehran University of Medical Sciences, Tehran, Iran
[c] Research Center for Biomedical Technology and Robotics, Tehran University of Medical Sciences, Tehran, Iran
[d] Geneva University Hospital, Division of Nuclear Medicine and Molecular Imaging, CH-1211 Geneva, Switzerland
[e] Geneva Neuroscience Center, Geneva University, CH-1205 Geneva, Switzerland
[f] Department of Nuclear Medicine and Molecular Imaging, University of Groningen, University Medical Center Groningen, 9700 RB Groningen, The Netherlands

ARTICLE INFO

ABSTRACT

There have been exclusive features for hybrid PET/MRI systems in comparison with its PET/CT counterpart in terms of reduction of radiation exposure, improved soft-tissue contrast and truly simultaneous and multi-parametric imaging capabilities. However, quantitative imaging on PET/MR is challenged by attenuation of annihilation photons through their pathway. The correction for photon attenuation requires the availability of patient-specific attenuation map, which accounts for the spatial distribution of attenuation coefficients of biological tissues. However, the lack of information on electron density in the MR signal poses an inherent difficulty to the derivation of the attenuation map from MR images. In other words, the MR signal correlates with proton densities and tissue relaxation properties, rather than with electron density and, as such, it is not directly related to attenuation coefficients. In order to derive the attenuation map from MR images at 511 keV, various strategies have been proposed and implemented on prototype and commercial PET/MR systems. Segmentation-based methods generate an attenuation map by classification of T1-weighted or high resolution Dixon MR sequences followed by assignment of predefined attenuation coefficients to various tissue types. Intensity-based segmentation approaches fail to include bones in the attenuation map since the segmentation of bones from conventional MR sequences is a difficult task. Most MR-guided attenuation correction techniques ignore bones owing to the inherent difficulties associated with bone segmentation unless specialized MR sequences such as ultra-short echo (UTE) sequence are utilized. In this work, we introduce a new technique based on statistical shape modeling to segment bones and generate a four-class attenuation map. Our segmentation approach requires a torso bone shape model based on principle component analysis (PCA). A CT-based training set including clearly segmented bones of the torso region of 20 clinical studies was designed. Using this training set, a bone atlas was trained taking advantage of PCA analysis. Our active shape segmentation technique uses the trained shape model to segment bones from user defined initial seed points. The segmentation algorithm was evaluated using 10 clinical datasets (aligned MR and CT pairs). The resulting attenuation maps were compared to corresponding attenuation maps derived from CT resulting in a mean relative difference less than 7%.

© 2013 Elsevier B.V. All rights reserved.

1. Introduction

Hybrid imaging systems enable the combination of functional and anatomical imaging modalities in a single session. During the last decade, hybrid PET/CT systems have evolved rapidly and achieved widespread acceptance to become one of the standard diagnostic imaging tools in clinical practice [1,2]. The recent introduction of hybrid PET/MRI systems, a technology enabling to combined molecular PET imaging with multiparametric MR signals, stimulated the interest of the medical imaging community given the many advantages they offer compared to PET/CT including the improved soft tissue contrast of MR compared to CT and reduced radiation dose to the patient [3].

A number of strategies have been recently proposed to perform MR-based attenuation correction [4–6]. Among these techniques, segmentation (tissue classification)-based methods are the most popular and practical approaches. The approach adopted on the

* Corresponding author at: Tehran University of Medical Sciences, Research Center for Molecular and Cellular Imaging, Pour sina, Tehran, Iran.
Tel.: +989125789765.
E-mail address: mohammadreza_ay@tums.ac.ir (M. Reza Ay).

Philips Ingenuity PET/MR system uses a 3D multi-stack spoiled T1-weighted gradient echo sequence to partition MR images in a finite number of classes (soft-tissue, lung and air). Thereafter, attenuation coefficients at 511 keV corresponding to biological tissues of each class are assigned to voxels belonging to this class [4,7]. This category of methods is challenged by the difficulty associated with segmenting bones from corresponding MR images since bones and air cavities have identical signal intensity in MR images when using conventional sequences. The lungs are well shaped organs and as such, popular segmentation algorithms enable their successful classification. However, bony structures contain a thin layer of low intensity cortical bone which encompasses a very high intensity bone marrow signal, thus making it very difficult to delineate them through an image segmentation approach.

Specially designed pulse sequences such as ultra-short echo (UTE) [8,9] and a combination of short echo-time (STE) and long echo-time (LTE) [10] enabling to differentiate between bones and air cavities have been suggested recently. However, this approach is practical only for scans covering a limited axial field-of-view (e.g. brain or head and neck) owing to the long acquisition time for whole-body imaging. For torso PET/MR imaging, bony structures are usually ignored and considered as soft tissue, assuming that neglecting bones does not significantly affect quantitative PET imaging [7]. The validity of this hypothesis was evaluated by several groups demonstrating that ignoring bone might not be adequate for quantification of osseous lesions. This is particularly a concern in therapy monitoring applications. A wide range of standardized uptake value (SUV) underestimation for osseous lesions was reported in the literature. The bias was reported to be 5–15% [7,11,12] or up to 23% [13] when PET/CT data is used, whereas simulation studies using an anthropomorphic thorax phantom reported a local bias of up to 17% [14] or even 30% [15].

Image segmentation, which has been identified as the key problem of medical image analysis and remains a popular and challenging area of research, is the process of extracting the object of interest from its neighborhood (e.g. bones in the torso region). The most challenging issue in this particular context is that direct bone segmentation using MR image intensities is a very difficult task. Nevertheless, a limited number of papers reported on techniques enabling to segment bone from MR images for some regions of the body based on 2D or 3D local texture information and also local 3D histograms analysis [16–19].

Fortunately for medical imaging applications, the shape and location of major bones are well identified from knowledge of the human anatomy. This knowledge can be included during the segmentation process to model bone shape parameters. A straightforward approach to incorporate this prior knowledge consists in probing a number of training shapes using statistical shape modeling approaches [20]. In this work, we propose a new segmentation technique based on statistical shape modeling to segment bones from MR images in combined torso PET-MR imaging, thus enabling to generate a 4-class attenuation map (background, lungs, soft tissue, and bone) at 511 keV.

2. Materials and methods

2.1. Statistical atlas generation

The generation of a statistical atlas is a common prerequisite for shape-based segmentation procedures. A statistical atlas represents a statistical distribution of object's shape in space whose components are detected using multivariate analysis techniques such as principle component analysis (PCA) on training sets. Our training set was produced from torso CT scans of 20 patients.

In the first step, bones of the torso region are segmented using connected thresholding. Connected thresholding methods label voxels connected to an initial seed when they lie within a lower and upper threshold. Voxel having intensities higher than 120 HUs were assumed to belong to bony regions. The result of this step is a binary mask where bones are assigned label 1 and the remaining regions label 0. In the second step, a special distance map referred to as "signed distance map" (SDM) is calculated on the segmented object (bones). In this process, the Euclidean distance of each voxel from the segmented object boundary is calculated and the result assigned to that voxel. If the voxel is inside the segmented object, a negative calculated distance is assigned and vice versa. Danielsson's algorithm was used for the computation of image distance map [21].

The third step consists in performing rigid-body registration of the clinical studies used to build the atlas. The rigid registration algorithm uses 7 parameters: one isometric scale parameter for x, y and z coordinates, 3 rotational parameters and 3 shift parameters. The similarity metric used for registration is based on normalized correlation coefficients. To this end, one of the studies was selected as reference (target) while the remaining 19 floating images were registered to this target image. It is worth pointing out that the registration was performed on the images resulting from the application of the second step (SDMs). The final step consists of PCA analysis on shapes or rigidly registered SDMs. Briefly, PCA is the process of finding the most significant Eigenvalues of the covariance matrix. After sorting the calculated Eigenvalues, the 14 most powerful components are selected to form the shape space. The statistical atlas is then constructed using the calculated components (Fig. 1).

(a)　(b)　(c)　(d)　(e)　(f)　(g)
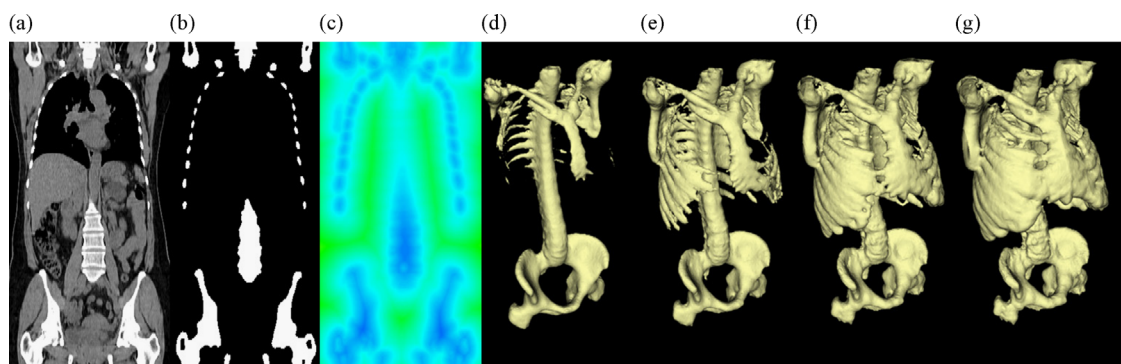
Fig. 1. Summary of steps required to generate the statistical atlas: (a) CT image of one patient from the training set, (b) bones extracted from the CT image, (c) signed distance map for segmented bones of the CT image, ((d)–(g)) generated torso bone shapes from the variation of the first component of shape space (increasing component values from left to right).

2.2. Shape-based segmentation

Geodesic active contours segmentation with shape guidance is a semiautomatic image segmentation algorithm which considers initial user specified seed points and a statistical atlas to segment the object [22]. The algorithm was implemented using the ITK class library. In brief, the user selects a number of seed points inside bones using an interactive user interface in order to segment bones. Subsequently, the edges are detected on the MR image (whose bones are to be segmented) to produce the so-called feature image (other features can be considered as well). In the following step, the fast marching algorithm is applied to the feature image through initialization from the selected seed point coordinates. As the model grows, its global properties are controlled using the rigidly transforming statistical atlas (constructed in the previous step) and other shape characteristics.

The Geodesic active contour shape prior level set image filter ITK filter was used for shape segmentation. This filter inherits active contour controlling parameters such as advection and curvature of the contour. These parameters were determined based on their concepts along with fine tuning following several tests. In addition to these parameters, the filter uses the statistical atlas to control the shape. In this case, the atlas holds 14 components, each one being controlled by one parameter. During this procedure, the filter finds the optimum 14 parameters to form the best fit shape.

The statistical shape model is not inherently capable of supporting rotation, scaling and translation of shapes. Therefore, a rigid spatial transformation using 7 parameters was added to the procedure. Twenty-one parameters (14 for shape model and 7 for transformation) in total were updated at each iteration of the segmentation process, which converged within 250–400 iterations.

A set of registered CT and MR image pairs of 10 clinical datasets were used to evaluate the proposed segmentation algorithm. The segmented bones from CT and MR images (using the proposed method) were compared using the "distance error map". This map (reported in mm) highlights the minimum distance of the surface voxel from one object to the other. The average error is referred to

as the distance error while the maximum error corresponds to the well-known Hausdorff distance [23].

In addition to the bones, it is necessary to segment lungs and soft tissue to generate a four-class attenuation map consisting of the background, lungs, soft tissue, and bone. The lungs were segmented using a connected region growing technique based on user selected seed points. The appropriate threshold for the lungs was estimated according to the intensity of seed points and their neighborhood voxels. A combination of Gaussian smoothing region growing and binary image morphology operators was used to separate the whole-body from the background. The minimum threshold for the whole body was selected to be above the maximum threshold of the lungs. Unwanted little gaps were filled using morphological operators.

The three different class (bones, lungs and soft tissue) were combined such that the voxels classified as being part of the whole-body but not labeled as bone were considered to belong to soft tissues class. Voxels belonging to bone and lung classes remained unchanged.

Following segmentation, attenuation coefficients at 511 keV were assigned to each specific class. The attenuation coefficients at 511 keV were assigned according to coefficients used in the XCAT anthropomorphic model [24,25]. The resulting attenuation map is then down-sampled and smoothed to produce the final attenuation map to be used for attenuation correction of the corresponding PET data.

3. Results

Image segmentation results using the proposed algorithm are shown in Fig. 2 where the voxels labeled in white were superimposed on the original MR image. The distance error map calculated on the corresponding CT-based bone segmentation is also shown (Fig. 2d). It should be noted that owing to the limited axial MR FOV, multiple volumes were merged resulting in slight visible mismatch (Fig. 2).
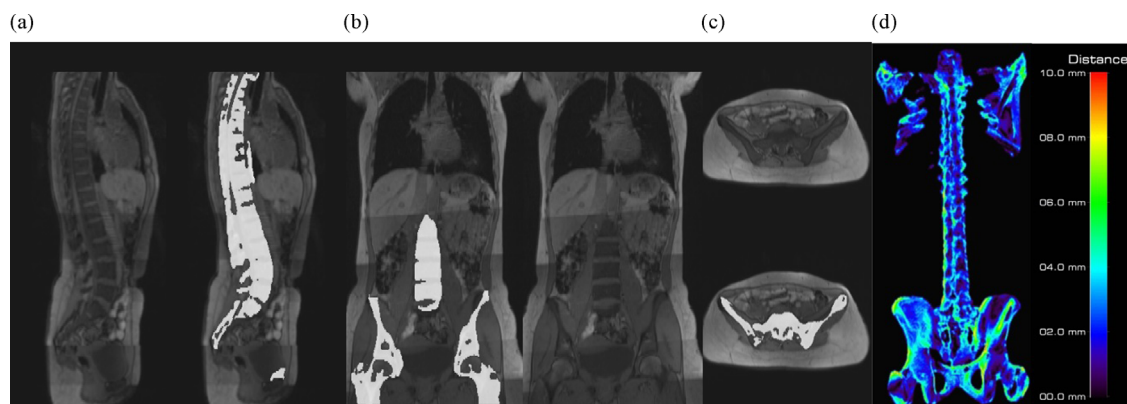

Fig. 2. Bone segmentation from MR images for one a clinical study shown on different views: (a) sagittal, (b) coronal, (c) and axial. (d) Distance error map calculated from comparison of MR segmented bones with CT segmented bones.

Table 1
Mean/standard deviation/maximum distance error between segmented MR bones from corresponding segmented CT bones for 10 clinical studies.

	P#1	P#2	P#3	P#4	P#5	P#6	P#7	P#8	P#9	P#10
Mean (mm)	6.26	5.08	3.19	4.86	5.67	5.04	4.93	6.52	3.9	7.59
Standard deviation (mm)	5.9	4.93	3.22	4.76	5.81	4.6	4.47	6.04	3.64	6.96
Max (mm)	34.54	30.29	21.51	28.46	34.1	27.54	27.68	30.95	30.63	34.44
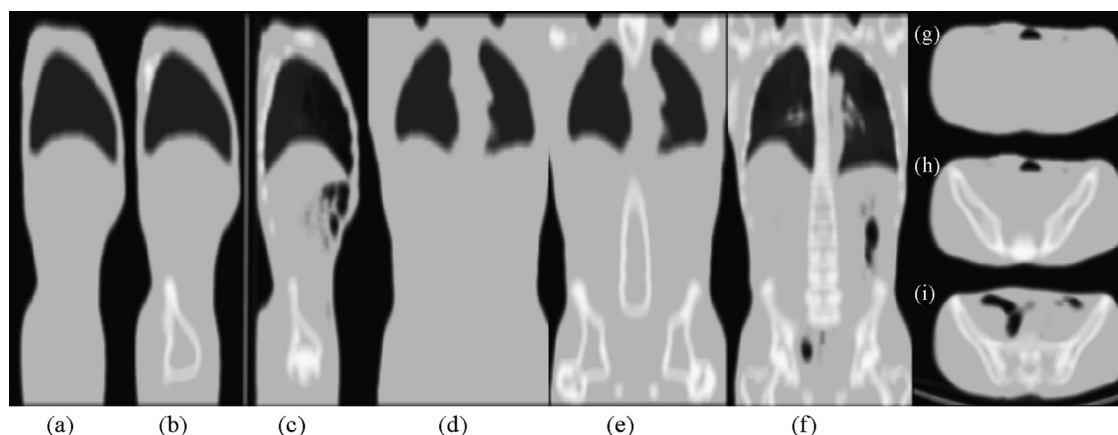
Fig. 3. Sagittal, coronal and axial views of the generated attenuation maps derived from MR and CT images. ((a), (d), (g)) 3-class μ-map derived from MR (soft tissue, lungs, and background), ((b), (e), (h)) 4-class μ-map derived from MR using our method (soft tissue, lungs, background and bone), ((c), (f), (i)) equivalent 4-class μ-map generated from CT.

Table 1 summarizes the distance error map between segmented bones from MR images using the proposed algorithm and those segmented from CT images, serving as reference for the 10 clinical studies used in this work. The mean error varies between 3 and 7 mm while the maximum error falls within the range of 21–35 mm.

Fig. 3 displays the MR-guided μ-maps generated using both the conventional 3-class (ignoring bone) and the 4-class approaches (considering bone) as compared to the reference CT-based attenuation map.

4. Discussion

In this work, we implemented a semiautomatic shape-based segmentation algorithm to extract bony structures from conventional T1-weighted MR sequence in order to generate an MR-guided attenuation map at 511 keV that can be used for attenuation correction of corresponding PET data on hybrid PET/MR system. The accuracy of the method was evaluated using aligned MRI and CT image pairs of 10 patients using the distance error metric [26].

The inclusion of bones will improve the quantitative capability of hybrid PET/MR imaging. The conclusions drawn from our previous work seem to suggest that classification of bones as a distinct class will compensate for tracer uptake bias of up to 17% in osteo-metastatic lesions [15]. Among the limitations of the proposed segmentation method is that it fails to segment rib bones owing to large shape variations between individuals (Fig. 2). However, since the ribs consist of thin bony structures, this shortcoming is not expected to produce severe bias in tracer uptake. Our reported mean and maximum error distances are large compared to previous related works on pelvic and femur bone segmentation from MR images (8 mm vs. 2 mm and 35 mm vs. 20 mm, respectively) [27,28]. This is likely due to the larger axial field-of-view and more complex segmentation of the torso region. Moreover, the femur and hip shape variations are less compared to the torso.

The downsampling and smoothing of the attenuation map to match PET's spatial resolution reduces the effect of segmentation and other errors as well as overestimation of bony structures in the attenuation map and corresponding ACF sinograms [29]. Using theoretical attenuation coefficients of biological tissues, a 4-class attenuation map including bone was produced using the proposed approach that enables to reduce the bias associated with attenuation correction errors in comparison with currently used 3-class attenuation maps ignoring bone.

5. Conclusion

This work proposes a novel approach to generate 4-class attenuation maps (background, soft tissue, lungs, and bone) for MR-guided attenuation correction on hybrid PET/MR systems. Attenuation correction methods ignoring bony structures used on current whole-body PET/MR systems cause the underestimation of tracer uptake especially in bony lesions, which might in some cases jeopardize clinical interpretation. Our proposed approach enables to classify bones for more accurate derivation of the attenuation map. Bone segmentation from conventional MR pulse sequences without the need to use sophisticated and time consuming special MR sequences reflects the novelty of our work. The suggested approach will undoubtedly improve the quantitative capability of PET/MR imaging in the clinic.

References

[1] D.A. Torigian, H. Zaidi, T.C. Kwee, B. Saboury, J.K. Udupa, Z.-H. Cho, A. Alavi, Radiology 267 (2013) 26.
[2] B.J. Pichler, H.F. Wehrl, A. Kolb, M.S. Judenhofer, Seminars in Nuclear Medicine 38 (2008) 199.
[3] H. Zaidi, A. Del Guerra, Medical Physics 38 (2011) 5667.
[4] M. Hofmann, B. Pichler, B. Scholkopf, T. Beyer, J. Eur, Nuclear Medicine and Molecular Imaging 36 (Suppl. 1) (2009) S93.
[5] H. Zaidi, Radiology 244 (2007) 639.
[6] G. Wagenknecht, H. Kaiser Jr, F. Mottaghy, H. Herzog, Magnetic Resonance Materials in Physics, Biology and Medicine 26 (2013) 99.
[7] A. Martinez-Moller, M. Souvatzoglou, G. Delso, R.A. Bundschuh, C. Chefd'hotel, S.I. Ziegler, N. Navab, M. Schwaiger, S.G. Nekolla, Journal of Nuclear Medicine 50 (2009) 520.
[8] V. Keereman, Y. Fierens, T. Broux, Y. De Deene, M. Lonneux, S. Vandenberghe, Society of Nuclear Medicine 51 (2010) 812.
[9] Y. Berker, J. Franke, A. Salomon, M. Palmowski, H.C. Donker, Y. Temur, F.M. Mottaghy, C. Kuhl, D. Izquierdo-Garcia, Z.A. Fayad, F. Kiessling, V. Schulz, Society of Nuclear Medicine 53 (2012) 796.
[10] P. Khateri, H. Salighe Rad, A. Fathi, M.R. Ay, Detectors and Associated Equipment 702 (2013) 133.
[11] Hu Z., Ojha N., Renisch S., Schulz V., Torres I., Pal D., Muswick G., Penatzer J., Guo T., Boernert P., Tung C.-H., Kaste J., Shao L., Morich M., Havens T., Maniawski P., Schaefer W., Guenther R., Krombach G. IEEE Nuclear Science Symposium & Medical Imaging Conference 2009, 3508.
[12] V. Schulz, I. Torres-Espallardo, S. Renisch, Z. Hu, N. Ojha, P. Börnert, M. Perkuhn, T. Niendorf, W. Schäfer, H. Brockmann, T. Krohn, A. Buhl, R. Günther, F. Mottaghy,

G. Krombach, European Journal of Nuclear Medicine and Molecular Imaging 38 (2011) 138.

[13] A. Samarin, C. Burger, S.D. Wollenweber, D.W. Crook, I.A. Burger, D.T. Schmid, G.K. von Schulthess, F.P. Kuhn, European Journal of Nuclear Medicine and Molecular Imaging 39 (2012) 1154.

[14] V. Keereman, R.V. Holen, P. Mollet, S. Vandenberghe, Medical Physics 38 (2011) 6010.

[15] A. Akbarzadeh, M.R. Ay, A. Ahmadian, N. Riahi Alam, H. Zaidi, Annals of Nuclear Medicine 27 (2013) 152.

[16] Xie T., Zaidi H. Eur J. Nuclear Medicine and Molecular Imaging 2013, in press.

[17] Mehranian A., Ay M., Rahmim A., Zaidi H. IEEE Transactions on Medical Imaging 32 (2013) 1707.

[18] Kapur T., Beardsley P., Gibson S., Grimson W., Wells W. Proceedings of the IEEE International Workshop on Model-based 3D Image Analysis 1998, 97–.

[19] Juneja P., Evans P., Harris E. IEEE Transactions on Medical Imaging 32 (2013) 1481.

[20] Z. Deak, J.M. Grimm, M. Treitl, L.L. Geyer, U. Linsenmaier, M. Korner, M.F. Reiser, S. Wirth, Radiology 266 (2013) 197.

[21] P.-E. Danielsson, Computer Graphics and Image Processing 14 (1980) 227.

[22] Leventon M.E., Grimson W.E.L., Faugeras O. Computer vision and pattern recognition, in: 2000 Proceedings IEEE Conference on 1 2000, 316 vol. 311.

[23] W.R. Crum, O. Camara, D.L.G. Hill, IEEE Transactions on Medical Imaging 25 (2006) 1451.

[24] W.P. Segars, M. Mahesh, T.J. Beck, E.C. Frey, B.M. Tsui, Medical Imaging 35 (2008) 3800.

[25] W.P. Segars, G. Sturgeon, S. Mendonca, J. Grimes, B.M. Tsui, Medical Physics 37 (2010) 4902.

[26] A. Akbarzadeh, D. Gutierrez, A. Baskin, M.R. Ay, A. Ahmadian, N. Riahi Alam, K. Lovblad, H. Zaidi, Journal of Applied Clinical Medical Physics 14 (2013) 238.

[27] M. Katsura, J. Sato, M. Akahane, I. Matsuda, M. Ishida, K. Yasaka, A. Kunimatsu, K. Ohtomo, European Journal of Radiology 82 (2013) 356.

[28] J. Schmid, N. Magnenat-Thalmann, Medical Image Computing and Computer-Assisted Intervention 11 (2008) 119.

[29] M. Ay, H. Zaidi, J. Eur, Nuclear Medicine and Molecular Imaging 33 (2006) 1301.